Sun-to-thermosphere simulation of the 28–30 October 2003 storm with the Space Weather Modeling Framework

Gábor Tóth,[1] Darren L. De Zeeuw,[1] Tamas I. Gombosi,[1] Ward B. Manchester,[1] Aaron J. Ridley,[1] Igor V. Sokolov,[1] and Ilia I. Roussev[2]

Received 26 July 2006; revised 23 March 2007; accepted 23 March 2007; published 13 June 2007.

[1] In late October and early November 2003 a series of some of the most powerful solar eruptions ever registered shook the heliosphere. These ''Halloween storms'' damaged 28 satellites, knocking two out of commission, diverted airplane routes, and caused power failures in Sweden, among other problems. This paper presents a 4-day end-to-end simulation of one of the major events (following the X17 flare) that produced the most geoeffective interval of the Halloween storm. The simulation was carried out with the newly developed Space Weather Modeling Framework (SWMF, see http://csem.engin.umich.edu/SWMF) that self-consistently couples physical domain models spanning from the solar corona to the upper atmosphere. The various attempts and iterations leading to the final simulation are also described. We briefly discuss the technological advances enabling the faster than real-time operation of the SWMF with the required high resolution. We compare the simulation results with observations from space- and ground-based measurements. We have also performed a reference magnetospheric simulation driven by ACE and Geotail observations and compared its results with the Sun-to-thermosphere simulation and the magnetospheric observations. The magnetic structure of the coronal mass ejection (CME) observed at the L1 point on the ACE spacecraft is not correctly reproduced because of the insufficient observations and theoretical understanding of the CME initiation mechanism. On the other hand, we find that the SWMF reasonably well reproduced both the hydrodynamic characteristics of the coronal mass ejection and some of the major indexes characterizing the strength of the geomagnetic storms.

Citation: Tóth, G., D. L. De Zeeuw, T. I. Gombosi, W. B. Manchester, A. J. Ridley, I. V. Sokolov, and I. I. Roussev (2007), Sun-to-thermosphere simulation of the 28–30 October 2003 storm with the Space Weather Modeling Framework, *Space Weather*, *5*, S06003, doi:10.1029/2006SW000272.

1. Introduction

[2] Satellites, global positioning systems, high-frequency communications, oil pipelines, and the electric power grid have all become facts of life; however, they all rely on technologies that can be negatively affected by conditions in the near-Earth space environment. In recognition of this, the National Space Weather Program (NSWP, see http://www.nswp.gov) was initiated to mitigate the adverse effects of space weather. The NSWP is a multiagency federal research program with NASA, NSF, NOAA, DoD, and DoE each playing major roles. The ultimate goal is to achieve timely, accurate, and reliable space environment observations, specifications, and eventually, forecasts. Thus understanding, modeling, and predicting the near-Earth space environment (geospace) remains a critical need for our society.

[3] The Sun-Earth system is a complex natural system of many different, interconnecting elements. The solar wind transfers significant mass, momentum, and energy to the magnetosphere, ionosphere, and upper atmosphere and dramatically affects the physical processes in each of these physical domains.

[4] The Center for Space Environment Modeling (CSEM) at the University of Michigan and its collaborators have recently built a Space Weather Modeling Framework (SWMF) [*Tóth et al.*, 2005]. The SWMF is designed to couple the models of the various physics domains in a flexible yet efficient manner, which makes faster than real-time space weather simulations feasible on massively parallel computers. Each model has its own dependent

[1]Center for Space Environment Modeling, University of Michigan, Ann Arbor, Michigan, USA.
[2]Institute for Astronomy, University of Hawaii at Manoa, Honolulu, Hawaii, USA.

variables, mathematical model, and numerical scheme with an appropriate grid structure and temporal discretization. The physics domains may overlap with each other or they can interact through a boundary surface. The SWMF is able to incorporate models from the community and couple them with modest changes in the software of an individual model. The efficient computational algorithms incorporated into the SWMF combined with the power of new supercomputing systems enable us to carry out realistic space weather simulations of the entire Sun-Earth system faster than real time (not counting human interactions, restarts, repeated runs, etc.). This paper presents the results of our simulation of about 4 days following one of the major solar events that produced some of the largest geoeffectiveness intervals in recent history.

[5] Idealized coronal mass ejections (CMEs) have been modeled from the Sun to the thermosphere by the CSEM [*Tóth et al.*, 2005] and the Center for Integrated Space Weather Modeling (CISM) groups [*Luhmann et al.*, 2004]. Simulations of real CMEs propagating through the solar corona to the location of Earth have also been done by several groups [*Wu et al.*, 1999; *Riley et al.*, 2002; *Usmanov and Goldstein*, 2003; *Manchester et al.*, 2004, 2005; *Odstrcil et al.*, 2005]. An event study of interacting CMEs has been completed recently with the heliospheric components of the SWMF [*Lugaz et al.*, 2007].

[6] There have been a large number of publications dedicated to the study of the Halloween eruptions. Here we mention some of the most relevant papers only. *Krall et al.* [2006] modeled the 28–30 October 2003 period with a 1.5-dimensional (1.5-D) MHD model for the CME. They have also coupled the heliospheric results with a 3-D magnetosphere code and compared it with simulations driven by the observed solar wind data. *Liu and Hayashi* [2006] modeled the CME eruption in the solar corona with simple density and pressure perturbations. *Dryer et al.* [2004] predicted the shock arrival times in real time with reasonable success.

[7] To the best of our knowledge, this is the first first-principles-based Sun-to-thermosphere simulation of a real event that was completed faster than real time. Although the results are far from being perfect, they are definitely promising. The simulation demonstrates the feasibility of modeling the whole Sun-to-thermosphere system with physics-based models, and it also shows the areas where improvements are needed. With further advances in the physics models, numerical algorithms, software development, and computational resources, first-principles-based space weather forecasting is becoming a realistic goal for the not too distant future.

[8] Modeling a superstorm has multiple purposes: (1) it validates the simulation against observations for an extreme event; (2) it tests the robustness of the SWMF for the most severe space weather events; and (3) it tests the speed of the SWMF for CMEs that reach the Earth much faster than typical. We have also modeled smaller, more typical events and even relatively steady conditions. These validation studies will be presented in other publications.

[9] The rest of this paper is organized as follows: The Halloween storm is described in more detail in section 2. The SWMF and its components are briefly discussed in section 3, and section 4 provides a description of the simulation and the various numerical techniques. The results are compared with the observed data in section 5. We conclude with a summary and an outlook for future development in section 6.

2. Halloween Storms

[10] In late October and early November 2003 a series of some of the most powerful solar eruptions ever registered shook the heliosphere [e.g., *Skoug et al.*, 2004; *Zurbuchen et al.*, 2004]. Dubbed "the Halloween storms," the blasts damaged 28 satellites, knocking two out of commission, diverted airplane routes, and caused power failures in Sweden, among other problems [*Barbieri and Mahmot*, 2004; *Getley*, 2004; *Lundstedt*, 2006; *Pulkkinen et al.*, 2005; *Webb and Allen*, 2004]. Long-distance radio communications were disrupted because of the effects on the ionosphere, and northern lights (aurora borealis) were seen as far south as Florida. The effects of the Halloween storms did not stop at Earth. They went beyond to burn out the radiation monitor aboard the Global Surveyor spacecraft orbiting Mars. That instrument had been tracking the radiation future explorers might encounter on trips to the Red Planet. Also, beyond Mars near the planet Saturn, the Cassini spacecraft measured the intense particle radiation from the Sun. Months later, the storms reached beyond Pluto's orbit to the edge of the solar system, washing over the Voyager spacecraft [*Intriligator et al.*, 2005].

[11] Solar flares are classified by the order of magnitude of the peak burst intensity measured at the Earth in the 1 to 8 band. The most powerful flashes are called "X-class" flares and they are characterized by the factor their peak intensity exceed the level of 10^{-4} Watts/m^2. The Halloween storms followed a 2-month quiet period with the emergence of active region 10484 producing an X1.1 flare on 19 October. During the next 5 weeks, two additional active regions, 10486 and 10488, produced some of the most intense flare activity and associated geomagnetic storms during Solar Cycle 23 [*Skoug et al.*, 2004]. While each of these regions were remarkable in size and magnetic complexity, region 10486 was by far the most significant. With a size exceeding 2600 millionths of the solar disk (over 13 times the size of Earth), region 10486 was the largest sunspot group observed since November 1990. It maintained its extreme size, complex magnetic structure, and thus great eruption potential, during its entire transit across the visible solar disk. Twelve of the 17 major eruptions that occurred during this period came from region 10486. Of the 12 major events, three stand out as defining events: the X17 on 28 October, X10 on 29 October, and X28 on 4 November

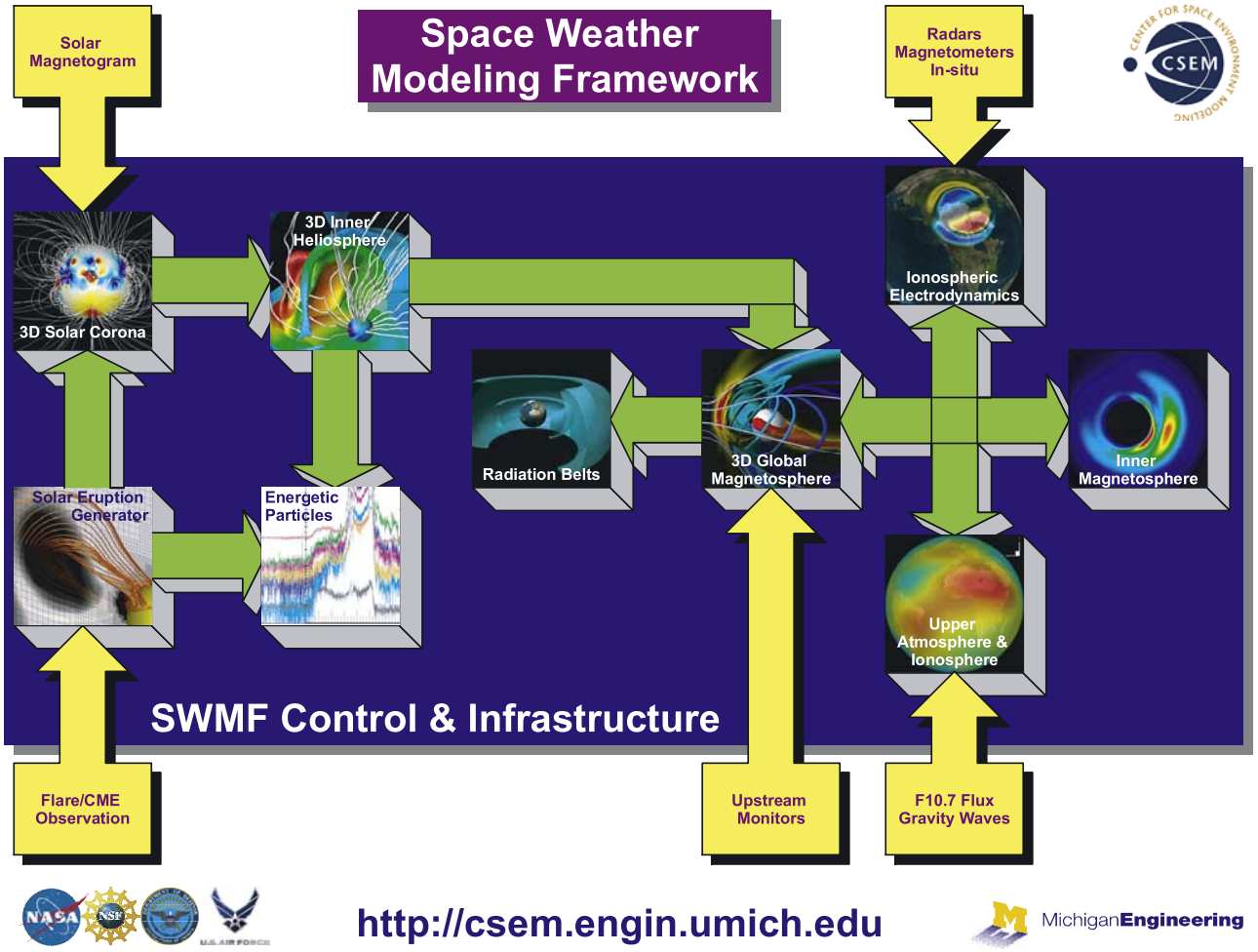

Figure 1. Space Weather Modeling Framework and its components. The arrows show the direction of data flow from observations to the components (yellow) and between components (green).

2003. Here we focus on the 28 October eruption that was the most geoeffective. The even larger 4 November eruption, fortunately, mostly missed the Earth.

3. Space Weather Modeling Framework

[12] In a number of fields in which computer-based modeling of complex, multiscale, multiphysics problems plays an important role, "software frameworks" are being developed. The term software framework lacks a unique definition: some groups refer to a collection of models that interact through a coupling mechanism, however simple or intricate the coupling, as a software framework; other groups refer to the coupling software itself, independent of the models that it can couple, as a software framework. *Killeen et al.* [2006] compare some of the frameworks developed by the space and Earth science community.

[13] The SWMF [*Tóth et al.*, 2005] is a flexible and expandable software framework for multicomponent physics-based space weather simulations, as well as for various other space physics applications. The SWMF integrates models of physics domains, ranging from the surface of the Sun to the upper atmosphere of the Earth. Each domain is described by an individually developed model, and the coupled models result in a self-consistent whole. The same physics domain may be represented by different models. In the framework the physics domains are represented by software components, and the models correspond to various component versions.

[14] The main design goals of the SWMF are (1) incorporate computational physics models with only modest modification; (2) achieve good parallel performance in the coupling of the physics components; and (3) allow the components to interact with the core of the SWMF as efficiently as possible.

[15] The SWMF is a fully functional and documented framework that provides a high-performance computational capability to simulate the physics from the low solar corona to the upper atmosphere of the Earth. Figure 1 shows the nine physics domains and the data flow between them. It also shows how the SWMF is driven by

external input data such as magnetograms, flare and CME observations, satellites upstream of the Earth (like ACE, Geotail, and Wind), etc. The SWMF is freely available via registration at http://csem.engin.umich.edu/SWMF.

3.1. SWMF Components

[16] The seven components used in the Halloween storm simulations are described in this section. The solar energetic particle model and the radiation belt components were not included because the corresponding models are not yet ready to be used in such a complex simulation. Many of the settings described below (like the grid sizes) are specific to this particular simulation and not fixed in the SWMF in general. The seven models used in the Halloween storm simulation are the following:

3.1.1. Solar Corona (SC)

[17] The Solar Corona domain is a Cartesian box that extends from the surface of the Sun to $-24\ R_S < x, y, z < 24\ R_S$, where R_S is the radius of the Sun. The physics of this domain is well approximated with the equations of magnetohydrodynamics. However, additional source terms are required to take into account the heating and acceleration of the solar wind [*Groth et al.*, 2000; *Usmanov et al.*, 2000]. Here we use the model presented by *Roussev et al.* [2003a] and incorporated into the BATS-R-US code [*Powell et al.*, 1999; *Gombosi et al.*, 2002, 2004].

[18] The inner boundary of the SC component is driven by the density, pressure, velocity, and magnetic field defined just above the transition region. The magnetic field is obtained from a synoptic solar magnetogram. The boundary conditions for the temperature and mass density at the Sun are varied with longitude and latitude to achieve the most realistic solar wind near the Sun and at 1AU. The velocity components at the inner boundary maintain line-tying of the magnetic field to the rotating solar surface. Differential rotation is currently neglected. The flow at the outer boundary is usually superfast (faster than the fast magnetosonic speed of the plasma), so no information is propagating inward.

3.1.2. Eruptive Event Generator (EE)

[19] The EE domain is embedded in the Solar Corona, and it is restricted to the region responsible for the eruptive event, or in other words, a coronal mass ejection (CME). The EE component can be represented as a boundary condition for the SC component or it can be a (nonlinear) perturbation of the SC solution. In short, the EE component interacts with the SC component only. Owing to the multitude of possibilities, the EE component is integrated into the SC component in the current implementation of the SWMF. Multiple EE versions are possible, but all the EE versions belong to one SC version only. In this work the EE model is a modified version of the *Titov and Dèmoulin* [1999] flux rope that is implemented in the BATS-R-US code [*Roussev et al.*, 2003b].

3.1.3. Inner Heliosphere (IH)

[20] The IH domain extends from its inner boundary at $r = 20\ R_S$ to a box with $-240\ R_S < x, y, z < 240\ R_S$. This box includes the orbit of the Earth. The physics of this domain is well approximated with the equations of ideal MHD. The IH component is usually solved in an inertial frame. We use the BATS-R-US code with an adaptive Cartesian grid to model this region.

[21] The inner boundary conditions of the IH component are obtained from the SC component. The flow at the outer boundary of the IH component is always assumed to be superfast (the interaction with the interstellar medium is outside of the IH). The IH model provides the upstream boundary conditions for the Global Magnetosphere (GM) component. The IH and GM domains overlap: the upstream boundary of GM is at about 32 $\mathbf{R}_E$ (Earth radii) upstream from the Earth, which is inside the IH domain.

3.1.4. Global Magnetosphere (GM)

[22] The GM domain contains the interaction region between the solar wind and the magnetized planet. The GM domain extends to 32 $\mathbf{R}_E$ on the dayside, 224 $\mathbf{R}_E$ on the nightside, and $-64\ \mathbf{R}_E < y, z < 64\ \mathbf{R}_E$ in the directions orthogonal to the Sun-Earth line. The physics of this domain is well approximated with the resistive MHD equations except near the planet, where it overlaps with the particle drift dominated Inner Magnetosphere (IM). We use the BATS-R-US code to model the GM domain.

[23] The upstream boundary conditions are obtained from the IH component or from satellite measurements propagated to the boundary. At the other outer boundaries zero gradient is assumed for the plasma variables since these boundaries are far enough from the planet to have no significant effect on the dynamics near the planet. In the present simulation the inner boundary of the Global Magnetosphere is at 2.5 $\mathbf{R}_E$ from the center of the planet. The inner boundary conditions are partially determined by the Ionosphere Electrodynamics (IE) component, which provides the electric potential (and thus the convection pattern) at the inner boundary of the GM. The potential is used to calculate the electric field and the corresponding plasma velocities, which are used as the inner boundary condition for the GM. The GM component also receives pressure and density corrections from the Inner Magnetosphere (IM) for the closed magnetic field lines (field lines connected to the planet at both ends). These values are used to ''nudge'' the MHD solution toward the more accurate inner magnetosphere values [*De Zeeuw et al.*, 2004].

[24] The GM component provides the field aligned currents to the IE component. These currents are mapped from the GM down to the ionosphere along the magnetic field lines. The Global Magnetosphere component provides the Inner Magnetosphere with the field line volume, average density, and pressure along closed field lines.

3.1.5. Inner Magnetosphere (IM)

[25] The IM domain consists of the closed field line region around the planet. This component solves equations describing the drift motion of the keV-energy ions and electrons. Kinetic effects are important for these particles, and the physics of this domain can be approximated in

different manners. In this work the Rice Convection Model (RCM) [*Wolf et al.*, 1982; *Toffoletto et al.*, 2003] is used that employs a two-dimensional bounce-averaged description of a multicomponent plasma with energy-dependent gradient and curvature drift.

[26] The Inner Magnetosphere obtains the geometrical and plasma information about the closed field lines from GM. It also obtains the electric potential solution from the Ionosphere Electrodynamics component. The IM component provides the density and pressure corrections along the closed field lines to the GM component.

3.1.6. Ionosphere Electrodynamics (IE)

[27] The IE domain is a two-dimensional height-integrated spherical surface at a nominal ionospheric altitude (at around 110 km for the Earth). We use the Ridley Ionosphere Electrodynamics Model (RIM) [*Ridley and Liemohn*, 2002; *Ridley et al.*, 2004] for the IE component.

[28] The IE component obtains the field aligned currents from GM, which is used to generate an auroral precipitation pattern. The Upper Atmosphere (UA) component provides IE with the Hall and Pedersen conductivities. The IE component provides the electric potential to the GM, IM, and UA components. In addition, it provides the particle precipitation to the UA component.

3.1.7. Upper Atmosphere (UA)

[29] The UA domain includes the thermosphere and the ionosphere and it extends from 90 km to 600 km altitude around the Earth. The physics of the Upper Atmosphere domain is approximated with the equations of multispecies nonhydrostatic hydrodynamics including viscosity, thermal conduction, photochemistry, chemical reactions, ion-neutral friction, coupling of the ions to the electric field, source terms due to solar radiation, etc. This domain is represented by the Global Ionosphere-Thermosphere Model (GITM) [*Ridley et al.* 2006].

[30] The lower and upper boundaries of the UA domain are approximated with physically motivated boundary conditions. The Upper Atmosphere model obtains the electric potential along the magnetic field lines and the particle precipitation from the Ionosphere Electrodynamics component. The gradient of the potential provides the electric field that is used to drive the ion motion, while the auroral precipitation is used to calculate ionization rates. The UA component provides the Hall and Pedersen conductivities to the IE component. The conductivities are calculated from the electron density and integrated along field lines.

3.2. MHD Model: BATS-R-US

[31] Three of the SWMF components (SC + EE, IH, and GM) are based on the BATS-R-US code [*Powell et al.*, 1999; *Gombosi et al.*, 2002, 2004]. The accuracy, efficiency, and robustness of BATS-R-US is crucial to the success of the SWMF simulations. This flexible global MHD code has the capability of modeling the Earth's magnetosphere, the solar corona, the inner and outer heliosphere, the magnetospheres of comets, Mars, Jupiter, and Saturn, and other magnetized and unmagnetized bodies.

[32] The BATS-R-US code solves the governing equations of magnetohydrodynamics. Nonideal MHD terms are included through appropriate source terms. The code uses a limited reconstruction that ensures second-order accuracy away from discontinuities, while simultaneously providing the stability that ensures nonoscillatory solutions. In addition, the code employs several approximate Riemann solvers. The resulting scheme solves for the hydrodynamic and electromagnetic effects in a tightly coupled manner, yielding a conservative scheme that works equally well across a range of several orders of magnitude in plasma β (the ratio of plasma pressure to magnetic pressure).

[33] In BATS-R-US a relatively simple yet effective block-based adaptive mesh refinement (AMR) is used in conjunction with a finite-volume scheme. The computational cells are embedded in regular structured blocks of equal-sized cells. The blocks are geometrically self-similar. Solution data associated with each block are stored in standard indexed array data structures. Computational grids are composed of many self-similar blocks. Adaptation is accomplished by the dividing and coarsening of appropriate solution blocks. In regions requiring increased cell resolution, a "parent" block is refined by dividing itself into eight "children" or "offspring." In regions that are deemed overresolved, the refinement process is reversed, and eight children are coarsened and coalesced into a single parent block. In this way, the cell resolution is changed by a factor of 2.

[34] One of the main limitations of most global magnetosphere codes is the explicit time-stepping algorithm. Explicit time steps are limited by the Courant-Friedrichs-Lewy (CFL) condition, which essentially ensures that no information travels more than a cell size during a time step. This condition represents a nonlinear penalty for highly resolved calculations, since finer grid resolution not only results in more computational cells but also in smaller time steps.

[35] We have implemented a fully implicit time-stepping scheme especially designed for good parallel performance [*Tóth et al.*, 2006]. We can also combine explicit and implicit time stepping. In global magnetospheric simulations the combined explicit-implicit time-stepping scheme improves the speed of the BATS-R-US code by a factor of 20 or more.

3.3. Control and Coupling

[36] The models are coupled together by the framework including a control module that determines the overall time-stepping of the code, the parallel decomposition of the models, the initiation and termination of the model runs, and the saving of restart files of the models. The control module also determines when the coupling should occur, how it happens, it takes care of grid interpolation, message passing between different components, and syn-

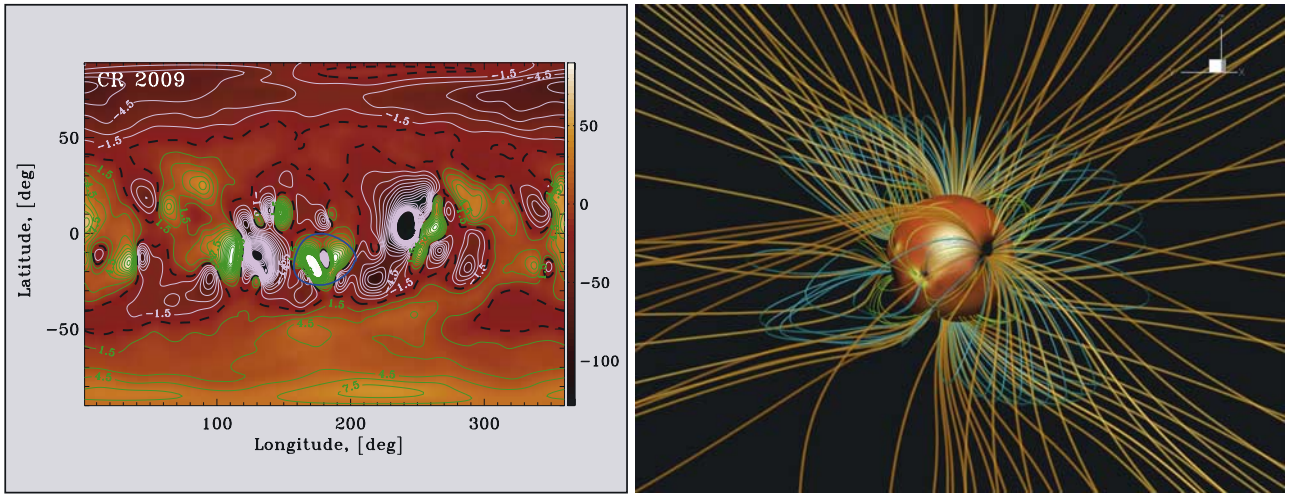

Figure 2. (left) Radial component of the magnetic field in Gauss (color scale, green and white contour lines for positive and negative values, respectively), the neutral lines (black dashed) and the active region 10486 that produced the (encircled with a blue line). (right) Resulting steady state magnetic field solution with closed (green and blue) and open field lines (orange). The surface of the Sun is colored according to the radial magnetic field.

chronization of the model runs to allow for a physically meaningful coupling. For sake of good parallel performance the processors are synchronized only when necessary. The coupling and execution scheduler avoids the possibility of deadlocks [*Tóth*, 2006].

[37] The SWMF can run both in time-accurate and steady state mode. In time-accurate mode all the participating components model the same time period and the coupling frequencies are based on simulation time. In steady state mode the components can run with different frequency and their couplings are based on iteration number rather than time. The steady state mode allows faster convergence to a steady state and/or a good initial condition.

[38] Finally, the coupling between components can also be crucial for the efficiency of the whole SWMF. The coupling between the GM/BATSRUS and IM/RCM models involves the tracing of the closed field lines in the GM domain. This is very time consuming if done with a straightforward and/or serial algorithm. We have developed an efficient parallel field line tracing algorithm [*De Zeeuw et al.*, 2004] to overcome this problem.

4. Halloween Storm Simulation

[39] We present simulation results for the 28 October 2003 eruption and the following geomagnetic storm. This was one of the most energetic CMEs ever observed: it was associated with an X17.2 flare. It appeared close to the central meridian of the Sun and it was very geoeffective.

4.1. Initial State

[40] The first step is to create the initial condition. We used a high-resolution (90th order spherical harmonics) MDI synoptic map centered around the time of the 28 October eruption to obtain a steady state solution in the SC component that is in a corotating coordinate system. We use the Heliographic (HGR) coordinate system with the sidereal Carrington rotation period of 25.38 days and an offset angle around the Z axis that places Earth in the $-X$, Z half plane at the eruption time of the 28 October CME (around 1054 UT). Since the coordinate system is rotating, the Coriolis and centrifugal forces are included when solving the MHD equations.

[41] The SC grid consists of blocks of $4 \times 4 \times 4$ cells. The small block size allows flexible adaptation. The computational grid is highly refined around the active region: the smallest cells are about 3×10^{-3} R_S only! This is necessary to obtain an energetic eruption from the active region without excessive numerical dissipation. We also refine the grid with 0.1 R_S cells inside a cylinder with 1 R_S diameter and an axis coinciding with the Sun-Earth line so that the solution propagating toward the Earth is well resolved. Thanks to the adaptive grid, the total number of cells remains only 2.7 million. Figure 2 shows the magnetogram and the steady state solution obtained from it. The convergence toward the steady state is greatly accelerated by the local time-stepping algorithm of the BATS-R-US code that uses different time step in each cell based on the local stability condition. About 25,000 iterations are sufficient to reach an accurate steady state solution.

[42] The next step is to obtain an initial condition for the heliosphere. The IH component is coupled to the SC component at the inner boundary of IH at 20 R_S. Since SC has already converged to a steady state, only IH needs to run. The flow is superfast throughout the heliosphere domain; thus it takes only about 2000 iterations with the

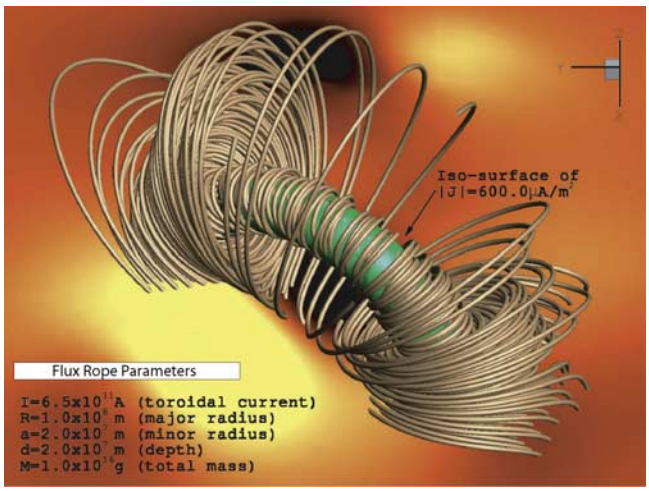

Figure 3. Three-dimensional view of the inserted flux rope superimposed to the background field of AR 10486.

local time-stepping algorithm to obtain a highly converged steady state solution for the given IH grid. During this initial setup the IH component uses a rotating coordinate system like the SC component so that a steady state can be obtained. During the time accurate part of the simulation, however, the IH component switches to the Heliographic Inertial (HGI) frame with an offset angle that puts the Earth in the $-X$, Z half plane (the orbital motion of the Earth is neglected). The rotational velocity $\Omega \times \mathbf{r}$ is added to the velocity when switching from the rotating to the inertial system.

[43] The IH grid is built up from blocks of $8 \times 8 \times 8$ cells each. The larger block size gives better performance. The grid resolution is 1/4 R_S near the inner boundary and also along the Sun-Earth line within a cylinder of 1 R_S radius. The cell sizes are kept 1/2 and 1 R_S out to 30 and 60 R_S radii, respectively. The largest cells are 4 R_S. The IH grid consist of a total of 16.5 million cells that is much larger than the SC grid. By separating the SC and IH domains, we gain a lot in computational efficiency: the SC grid needs a lot of iterations but it is relatively small, while the IH grid is huge, but it needs fewer iterations.

4.2. Generating Eruptive Events

[44] The 28 October event was preceeded by several smaller CMEs, which significantly modified the ambient solar wind. Our first simulations ignored this effect, and we launched the 28 October CME into the steady state solar wind. We found that the results were rather far from the observations: the CME arrived too late and the velocity jump was too small. To take into account the preconditioning effect of previous CMEs on the solar wind, we started the run from 26 October, when a smaller CME was launched at 0654 UT from the same active region (AR10486). Accidentally, in the simulation we used 0724 UT as the initiation time, but this half an hour difference is well within the uncertainties of the observations and the initial conditions and does not have a significant effect on the results.

[45] Vector magnetograms clearly show that the magnetic field of AR10486 is very highly sheared with the field running nearly parallel to the neutral line from which the CMEs erupt [*Liu and Hayashi*, 2006]. The evolution of magnetic shear is made manifest by observations of photospheric proper motions, which show strong shear flows along the magnetic neutral line prior to CMEs [*Yang et al.*, 2004]. These observations strongly suggest that the magnetic shear is driving the CMEs. A physically self-consistent simulation of such shear flows has recently been performed [*Manchester*, 2001], which shows that the flows are driven by the Lorentz force that occurs as the magnetic field emerges in a stratified atmosphere. Furthermore, these Lorentz-force-driven flows may persist until the magnetic field becomes so highly sheared that there is a loss of equilibrium resulting in a CME as shown by *Manchester* [2003]. Currently, we can not include such a self-consistent initiation mechanism in a global model because we cannot resolve the photospheric pressure scale height over such a large area. While we await for the observational and numerical capabilities to self-consistently model CMEs, we turn to flux ropes to drive eruptions that capture the energy and magnetic flux of a CME.

[46] The eruptions were initiated with the EE by inserting a realistic size flux rope (the size of the active region) based on the modified *Titov and Dèmoulin* [1999] model arching above the active region 10486 [*Roussev et al.*, 2003b] (see Figure 3). The location and orientation of the flux ropes were chosen to arch over the dipolar part of the active region. The active region can be easily identified in the high-resolution synoptic map obtained from the observed photospheric magnetic field. The density in the loop was obtained from the size and estimated mass of the CMEs. The magnetic field strength of the flux ropes were set so that the resulting eruptions match SHOHO/LASCO observations of the CME speeds at 20 solar radii (1500 and 2500 km/s for the 26 October and 28 October events, respectively). We determined this from a few relatively short runs.

[47] At the time of the first eruption we switched to time accurate mode. After 20 min of the start of the time-dependent simulation the leading shock of the first CME reaches a radial distance of 5.5 R_S at a speed slightly exceeding 2100 km/s. At this point the grid at the active region is coarsened by a factor of 4 so that the simulation can be run more efficiently. The first CME reaches the SC/IH boundary at 20 R_S after about 1.7 hours and the speed of the leading shock is the observed 1500 km/s. The first CME is propagating in a direction about 30 degrees off from the Sun-Earth line, but the flanks of the shock reach the Earth 45 hours after the eruption at 0430 UT 28 October. The solar wind velocity at the Earth increases from about 350 km/s to

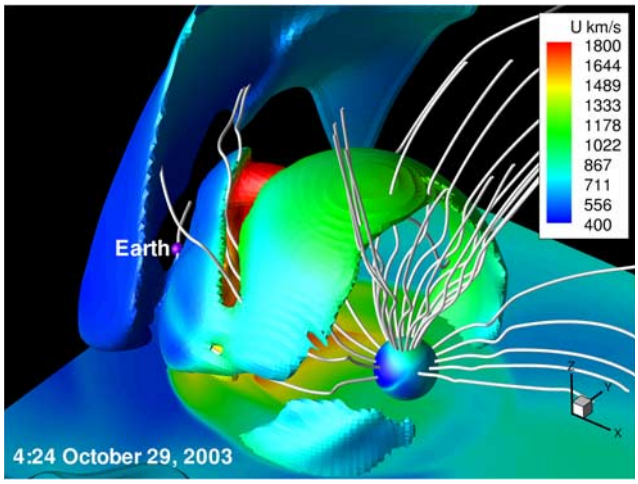

Figure 4. A snapshot of the heliosphere at 0424 29 October 2003. Disturbances are shown as isosurfaces where the density is increased by a factor of three over the ambient value. These surfaces are colored with the solar wind speed and they show the presence of shocks driven by the 26 October and 28 October coronal mass ejections (CMEs). A plane ($z = -40$ R_S) and sphere (inner boundary of inner heliosphere) are also shown colored to show flow speed. The location of the Earth is indicated with a blue sphere that is much larger than the actual size of the Earth. Gray lines illustrate the interplanetary magnetic field.

550 km/s, which is a good approximation to the solar wind conditions preceding the arrival of the 28 October CME as observed by the ACE satellite [*Skoug et al.*, 2004; *Zurbuchen et al.*, 2004].

[48] Before initiating the second CME, the active region is refined back to 3×10^{-3} R_S resolution at 1054 28 October. The flux rope is made 50% larger than the previous one and the magnetic field strength is increased so that the propagation speed of the CME reaches the 2500 km/s measured at 20 R_S. After 15 min the second CME propagates to 9 R_S and the shock speed is around 3200 km/s. Again, the grid near the active region is coarsened to speed up the simulation. The shock reaches the SC/IH boundary at 20 R_S in less than an hour with a speed around 2800 km/s.

[49] Even though the very high 3×10^{-3} R_S resolution is only used for 35 min of physical time, the time step becomes very small during this period and the simulation time can be very substantial. This problem becomes even more severe because this early phase of the eruption has to be simulated a couple of times to get the CME speed approximately agree with the LASCO observations at 20 R_S. Although we experimented with implicit time stepping, it did not speed up the simulation significantly, because the time step required by accuracy is not much larger than the stability limit for the explicit scheme.

[50] To overcome this problem we have developed a new partially steady-state algorithm that advances only a part of the computational grid, while the rest being in an approximate steady state is not evolved. Since BATS-R-US uses a block based grid, the computational grid is split into changing, boundary, and steady blocks. The boundary blocks are at the edge of the changing domain. The changing and boundary blocks are evolved, while the steady blocks are not. As soon as a boundary block starts to change significantly (e.g., the velocity changes by more than one part in a million) it is assigned to a changing status, and its neighbor becomes the new boundary. The changing and boundary blocks are load-balanced between the processors. This algorithm has sped up the simulation of initial phase of the CME eruption by a factor of 4 to 6. Surprisingly, the algorithm proved to be useful for launching the second CME as well because the SC solution has returned to an almost perfect steady state during the 2 days between the first and second CMEs. The second CME is faster than the first one, so it catches up with the wake of the first CME in the IH domain.

[51] For these extremely strong eruptions the temperature of the erupting plasma reached unphysically high values (over 10^9 K) in the simulations. This is most probably due to the unavoidable numerical resistivity that exceeds the resistivity of the plasma in the corona by many orders of magnitude. To mitigate this problem, we use an artificial cooling term that is switched on for temperatures exceeding 5×10^7 K with a characteristic cooling time of 100 s. This cooling eliminates the extremely high temperatures, but otherwise the solution does not change too much. The jump conditions at the shock are unaffected because the temperature at the shock is below 5×10^7 K. The very high temperatures that need to be controlled occur somewhat behind the shock front.

4.3. Propagation Through the Heliosphere

[52] Figure 4 shows the heliospheric solution when the second CME is reaching the Earth at 0430 29 October that is 17.5 hours after the eruption. This is about 1.8 hours earlier than the observed arrival time. The figure also shows that by this time the second CME almost catches up with the first one.

[53] The fastest plasma and strongest magnetic field of the second CME slightly missed the Earth. At Earth the velocity jumped from 450 km/s to 1200 km/s and the magnetic field components varied with 15 to 25 nT amplitude. The ACE observations [*Skoug et al.*, 2004; *Zurbuchen et al.*, 2004] showed a solar wind speed exceeding 2000 km/s and the largest amplitude variations in the magnetic field components exceeded 40 nT. The difference in the arrival time and the strength of the CME is not unexpected given the limited information for the initial condition, the somewhat ad hoc initiation of the CME, and the various approximations in the physics and the numerical algorithms.

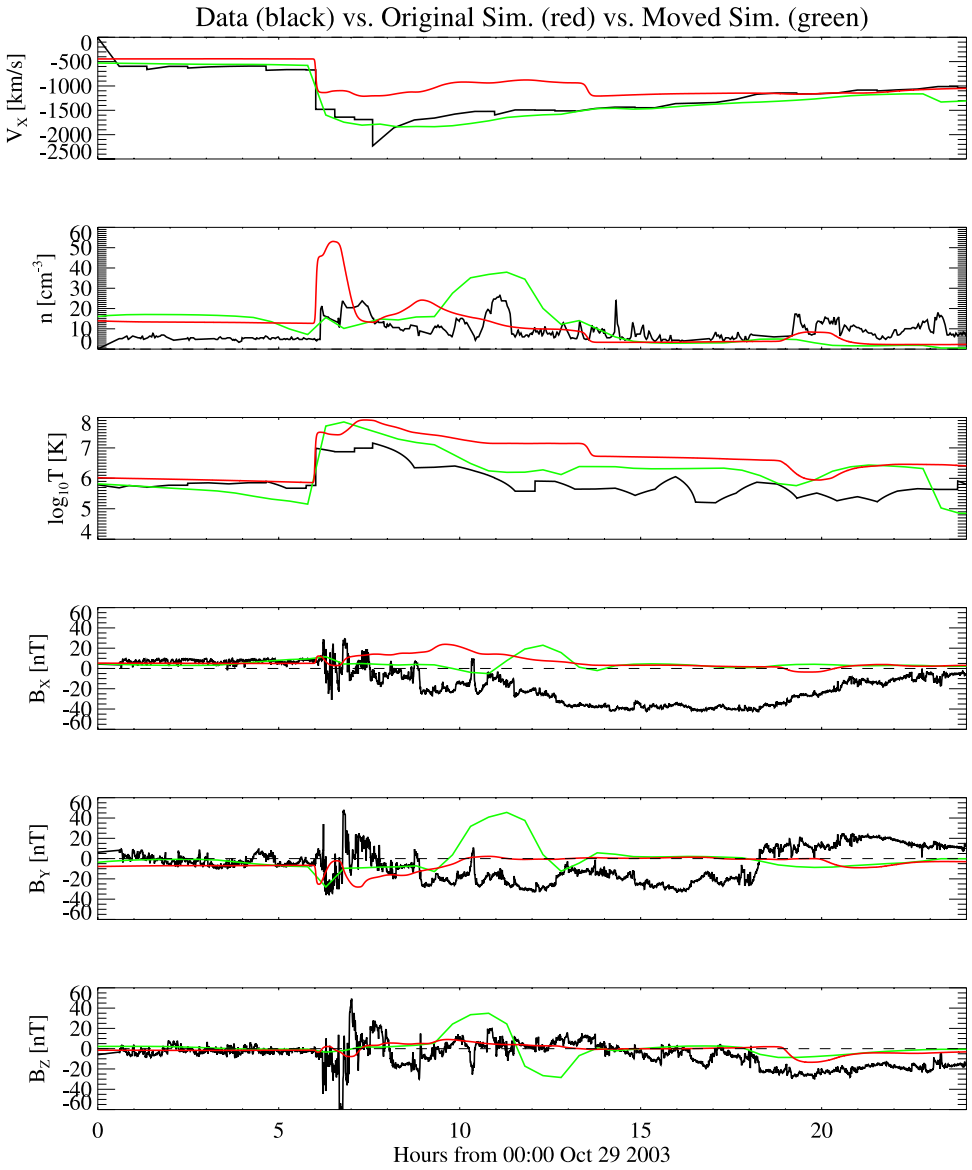

Figure 5. Comparison of the measured (black) and simulated (red and green) solar wind velocity, density, temperature, and magnetic field components. The measurements were obtained by the ACE (magnetic field, velocity, and temperature) and Geotail (density) satellites. The red line shows the simulated values at the position of the Earth, while the green line corresponds to a position shifted by 9° along the Earth orbit where the strongest part of the simulated CME was passing through. The simulations are time shifted by 1.8 and 3.4 hours, respectively, to match the observed arrival time of the shock.

[54] In order to improve the agreement between the simulation and observations, we moved Earth by 9° along its orbit where the strongest part of the simulated CME was passing through. Moving the Earth is an inexpensive alternative to true ensemble simulations. At this location the shock speed reaches 1800 km/s and the magnetic field varies in excess of 40 nT, which is in reasonable agreement with the observed values (see Figure 5). We also shifted the simulation time by 3.4 hours to match the observed arrival time of the shock.

[55] It is very interesting to note that with these adjustments the simulation gives a very good agreement with the observed velocity and a reasonable agreement with the observed density, temperature, and the magnetic field magnitude. However, the simulated magnetic field components do not agree with the observations. This implies that the simulated magnetic field topology does

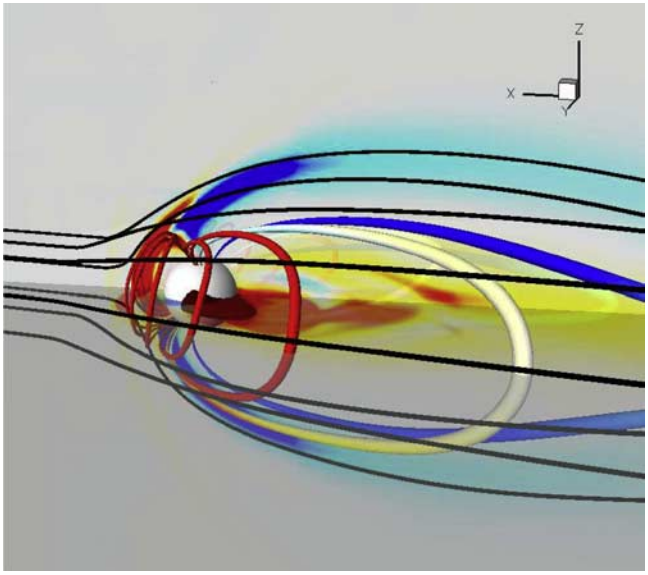

Figure 6. Three-dimensional structure of the magnetosphere in the Sun-to-thermosphere simulation 1 hour after the shock arrives at the Earth. The colored tubes show the last-closed magnetic field lines, while the black tubes indicate the solar wind flow around the magnetosphere. The color contours on the planes are electric current density. The 100 nPa pressure isosurface that intersects this boundary is shown in dark red.

not describe well the real CME. Realistically, this is not surprising, since the CME is initiated from an artificially inserted flux rope. Further research and more detailed observations will be needed to better understand the CME initiation mechanism and the physical and numerical reasons for the discrepancy in the magnetic field components.

4.4. Interaction of the CME with the Magnetosphere-Ionosphere-Thermosphere System

[56] So far the simulation used the SC and IH components only. We continue the simulation from a state a few hours before the October 28 CME reaches the Earth at its modified position, i.e., shifted by 9° along its orbit where the strongest part of the simulated CME was passing through. First, we obtain an approximate initial condition for the GM component using the IH solution as the upstream condition. Next, we produce an initial state for the coupled GM, IM, and IE components. GM/BATSRUS uses local time stepping with altogether 20,000 iterations, while IM/RCM runs in time accurate mode. The IE/RIM component is a Poisson solver that solves the equations instantaneously.

[57] The GM component uses an adaptive grid consisting of $8 \times 8 \times 8$ blocks with 1/4 $\mathbf{R}_E$ cells near the Earth and 8 $\mathbf{R}_E$ cells in the far tail, altogether about 1 million cells. The IM/RCM component runs on the standard nonuniform latitude-longitude grid with 78×48 cells, and the energy distribution of the various particles is represented by a total of 150 energy bins. The two dimensional IE/RIM grid has a uniform 1° resolution in latitude and longitude.

[58] Next, we switch to time accurate mode and run the IH, GM, IM, IE, and UA components fully coupled. The UA component is initialized with statistical models for the ionosphere and the thermosphere (MSIS and IRI). The spherical UA grid has a 5° resolution in longitude and latitude and 40 altitude levels between 95 km and 600 km. In time accurate mode the GM/BATSRUS component uses an implicit time-stepping scheme that is about 20 times faster than the explicit scheme. Furthermore, the SC component is only providing the inner boundary condition for IH, but otherwise it is not running. This can be done as long as the fully coupled run is shorter than the time it takes the solar wind to travel through the IH component. This is true if we are interested in the short term (less than a day) effects of the CME on the magnetosphere-ionosphere-thermosphere system. Switching off the SC component saves a lot of computational cost because SC is one of the most expensive components due to the very small time steps required by accuracy and numerical stability. The results of the Sun-to-thermosphere simulation will be analyzed in section 5.

4.5. Control Simulation Driven by Upstream Monitors

[59] To get a better handle on the source of errors in the full Sun-to-thermosphere simulation results, we have performed several simulations with various subsets of the GM, IM, IE, and UA components. In these control simulations the magnetosphere is driven at the inflow boundary by the solar wind data measured by the ACE

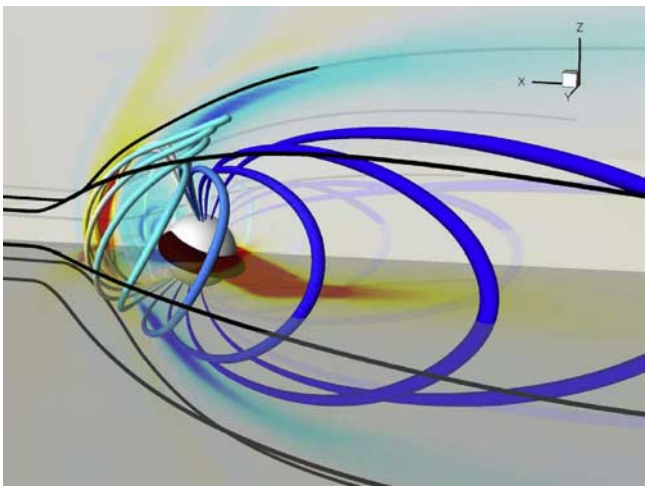

Figure 7. Same as Figure 6, except that here the satellite driven simulation data is used. The simulation time is 0700 UT on 29 October.

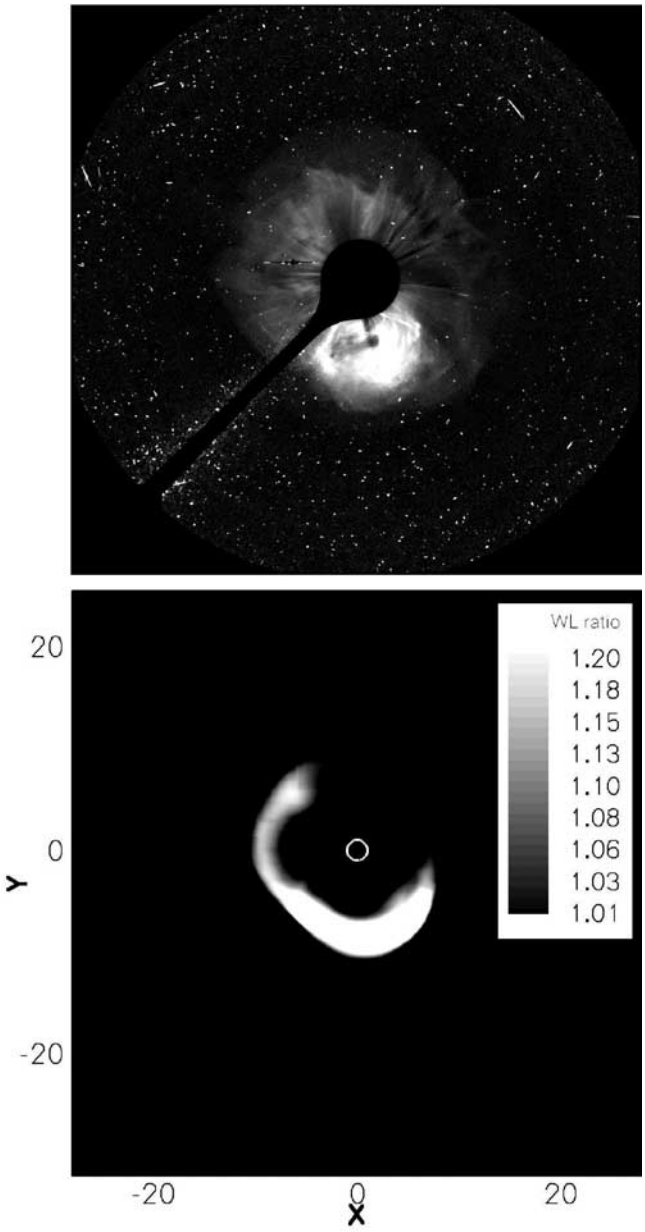

Figure 8. Comparison of the (top) observed and (bottom) synthetic white light images (white light ratio relative to the background). The observations were taken by the SOHO/LASCO C3 instrument somewhat more than an hour after the eruption. The synthetic image was obtained from the simulation 40 min after the 28 October eruption. The density ratio of the simulation results are divided by 1.55 for a better comparison, but otherwise the two images are on the same scale. Note the similarity of the sizes and shapes.

and Geotail satellites. Geotail data are used for density because the ACE plasma density data do not seem to be correct [*Skoug et al.*, 2004]: the density measured by ACE drops instead of increasing when the shock arrives. On the other hand the Geotail data show an approximately fourfold increase in the density [*Wang et al.*, 2005] as expected for a strong shock.

[60] The control simulations can help to distinguish between the errors due to the inaccuracies of the heliospheric components, and those made in the magnetosphere-ionosphere-thermosphere models in the full Sun-to-thermosphere simulation. While the control simulations are used here only as a tool to better understand the full Sun-to-thermosphere simulation results, we will analyze these satellite data driven simulations in much more detail, with quantitative validation against several observations, in future publications.

[61] Figures 6 and 7 show the 3-D representation of the magnetosphere about 1 hour after the shock arrival time for the Sun-to-thermosphere and the satellite driven reference simulations, respectively. Although there are obvious differences between the results, there are qualitative similarities. In both simulations there is a large ring current present (shown by the magenta isosurfaces in the figures), caused by a much larger ring current pressure than could be produced with MHD alone. This is due to the inclusion of a proper drift physics model (RCM). The large ring current pressure is essential for generating the proper Region 2 current system that connects the high-latitude ionosphere to the ring current. This coupling played an important role in driving the ionospheric convection pattern, and consequently, in controlling magnetospheric dynamics.

5. Validation of the Simulation Results

[62] In this section we compare the Sun-to-thermosphere simulation with observations and also with the control simulation driven by the observed solar wind data.

5.1. Validation of the Solar Corona and Heliosphere Results

[63] Figure 8 shows a comparison between the CME observed with LASCO C3 and a simulated white light image both made about 1 hour after the eruption. The simulated images are obtained by numerical integration of Thomson-scattered white light along the line-of-sight. Both the observational and synthetic plots are obtained from the total brightness divided by that of the preevent state. There is a good agreement in the overall size, shape, and brightness distribution. The amplitudes of the brightness ratios differ by about 50%. In the figure, the density ratio of the simulation results is reduced by 1.55 to allow a better comparison of the shapes and brightness distributions. A more detailed comparison study is in preparation (W. B. Manchester et al., 3D MHD simulation of the 2003 October 28 coronal mass ejection: Comparison and vali-

dation with white-light observations, to be submitted to *Astrophysical Journal*, 2007).

[64] The further propagation of the simulated CME to Earth can be validated by the comparison of the solar wind data measured at the Earth. As we have shown in Figure 5, the hydrodynamic parameters fit reasonably well after the position of the Earth is shifted along its orbit and the arrival time of the CME is matched with the observed time. The magnetic field components do not match, but the overall magnitude of the perturbations are reasonable. Comparison of Figure 4 with *Jackson et al.* [2006, Figure 6] also suggests that the simulated 3-D density structure qualitatively agrees with the density enhancements reconstructed from the Solar Mass Ejection Imager (SMEI) observations.

5.2. Validation of the Magnetosphere-Ionosphere-Thermosphere Results

[65] There are several planetary scale indices that characterize the overall dynamical state of the magnetosphere. Currently, it is fully expected that a Sun-to-thermosphere numerical simulation cannot describe the detailed dynamics at any given point of the magnetosphere-ionosphere system for several reasons: the boundary conditions at the Sun are not known accurately, the mechanism of the CME eruption is not understood, the numerical resolution is limited, and the governing equations lack some of the microphysics. Nevertheless, a high quality model should be able to reproduce global indices with reasonable accuracy.

[66] Figure 9 compares the simulation results with the assimilated ionospheric cross polar cap potential (CPCP) and the 1-min D_{st} index obtained from approximately 50 ground-based magnetometers spaced around the globe at low and middle latitudes. The method used to calculate the D_{st} index is described by *Lu et al.* [1998], although they only used 18 stations for the January 1997 event. Midlatitude stations can be included if the cosine of the latitude is considered. The D_{st} is calculated using an automated routine for 13 years and is available to the general public at http://amie.engin.umich.edu/. The CPCP is predicted by the assimilative mapping of ionospheric electrodynamics (AMIE) technique that were described by *Ridley and Kihn* [2004], in which AMIE results were compared to the Polar Cap Index over a 5 year time period. Figure 10.

[67] Figure 9 shows that the SWMF driven by the observed IMF does an extremely good job predicting these major indices even during the most disturbed periods. The CPCP values obtained with the AIME assimilative method and produced by the simulation follow each other quite closely. More importantly, the D_{st} index is directly obtained from ground magnetometer observations and it does not involve sophisticated data analysis. This index is also very well reproduced by the IMF driven simulation, particularly during the first part of the magnetic storm. The errors are somewhat larger when the observations are compared with the Sun-to-thermosphere simulation, but the results are still reasonable. If we regard this simulation result as a space weather forecast, the predicted ionosphere potential and D_{st} index could be a basis of a reasonably accurate warning about the severity of the coming magnetic storm.

[68] Finally, we compare the ion density observed by the Champ satellite with the results of the Sun-to-thermosphere simulation as well as with simulation results obtained with the stand-alone upper atmosphere model GITM driven by AMIE. Figure 10 shows that there is very good agreement between the observations and the stand-alone model, while the Sun-to-Earth simulation provides less accurate but still not unreasonable results.

[69] On the basis of the above validation study, we conclude that the errors of the Sun-to-thermosphere simulation are dominated by the inaccuracy of the simulated CME eruption and propagation and the numerical errors of the magnetosphere-ionosphere-thermosphere model are less significant.

6. Conclusion

[70] A Sun-to-thermosphere simulation of an observed space superstorm has been carried out for the first time. This simulation was made possible by the newly developed Space Weather Modeling Framework and its integrated models. The simulation was driven by observed synoptic solar magnetograms and with a flux-rope model of solar coronal mass ejections. The SWMF coupled seven models from the solar corona to the thermosphere.

[71] In the solar corona the speed and shape of the simulated CME agrees reasonably well with the SOHO/LASCO observations. On the other hand the shock arrival time at the Earth is off by about 2 to 3 hours, probably due to the inaccurate (too high) density of the ambient solar wind in the model. When the Earth is ''moved'' by about 9 degrees to the fastest part of the simulated CME, we find that the hydrodynamic characteristics (velocity, density, and temperature) agree reasonably well with the ACE observations at the L1 point. The magnetic field components do not agree with the measurements, but the amplitudes of the perturbations (about 40 nT) are comparable with the observed perturbations. This suggests that the magnetic energy of the CME is roughly correct, but the magnetic structure is not. Given the limited observations at the surface of the Sun and the relatively simple eruption initiation mechanism in the model, this is not too surprising. Although the magnetic structure is not reproduced, the strength and duration of the resulting geomagnetic storm is quite comparable with the observations. In particular, the simulated Dst index and the cross polar cap potential are fairly comparable with the observed values for almost 20 hours after the shock arrival.

[72] To identify the main source of error, we also carried out a control simulation of the magnetosphere-ionosphere-thermosphere system driven by the measured solar wind parameters. We found that this simulation gives excellent agreement with the magnetic field measurements by a suit of satellites located in different regions of geospace [*Gombosi et*

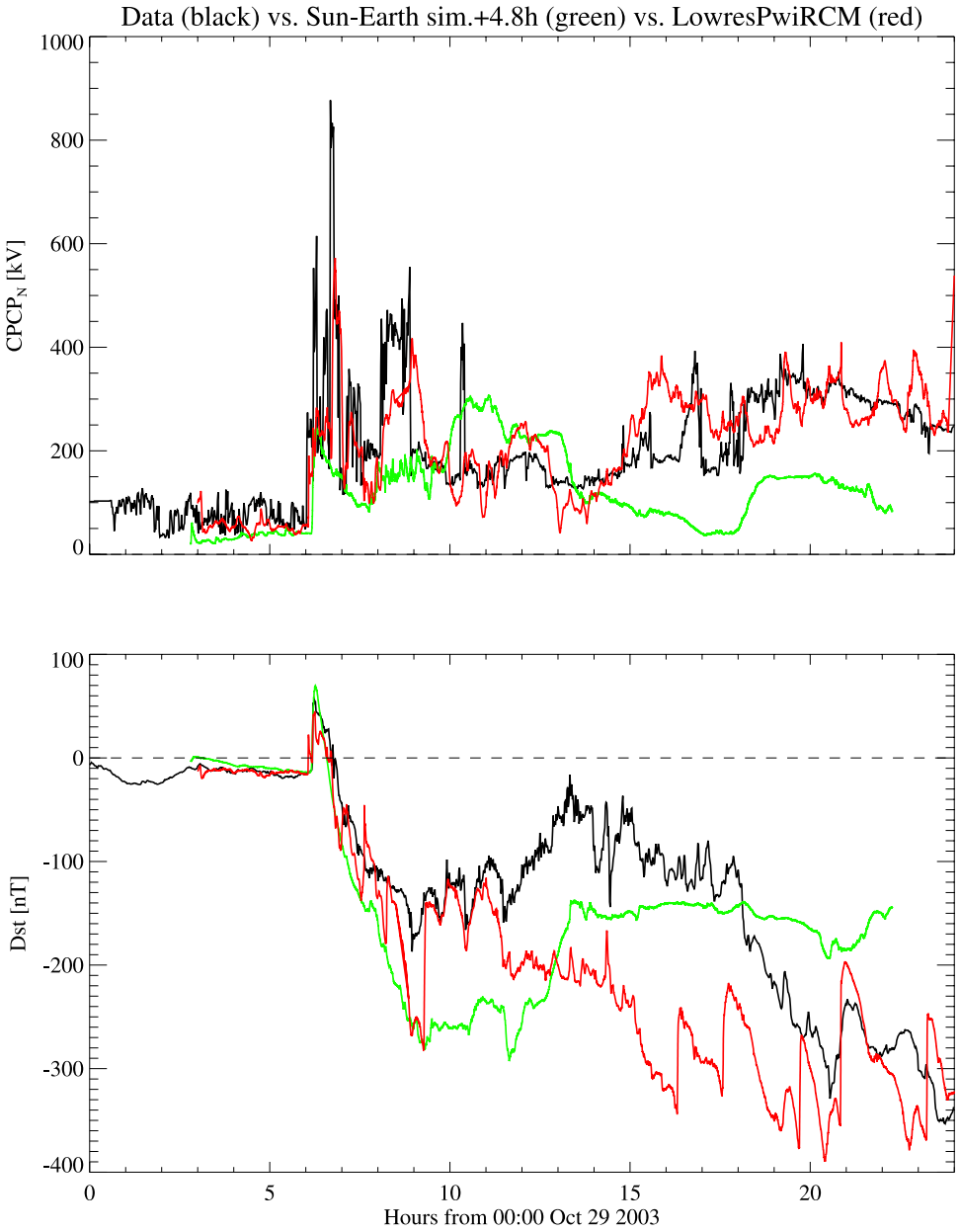

Figure 9. Assimilative mapping of ionospheric electrodynamics (AMIE) [*Lu et al.*, 1998; *Ridley and Kihn*, 2004] (black), magnetosphere-to-thermosphere simulation (red), and Sun-to-thermosphere simulation (green) results of the (top) ionospheric cross polar cap potential and (bottom) D_{st} for 29 October 2003.

al., 2006]. In addition, the global geomagnetic indices (like CPCP and D_{st} are also well reproduced by the simulation. We conclude that most of the errors originate from the solar corona, eruptive event generator, and heliosphere models. Most probably the error is dominated by the inaccurate model of the CME initiation.

[73] The Sun-to-thermosphere simulation demonstrates several important advances in modeling heliospheric storms. First, the CMEs were launched from realistically sized active regions due to the very high local resolution made possible by the adaptive grid. Without adaptive grids one must use unrealistically large active regions even when the code is run at high resolution. We also introduced a new "partially steady" numerical scheme to accelerate the computational speed. Second, we demonstrated that simulating the "preconditioning" of the heliosphere by earlier CMEs is very important if one wants to compare in situ observations with simulation results. Pre-

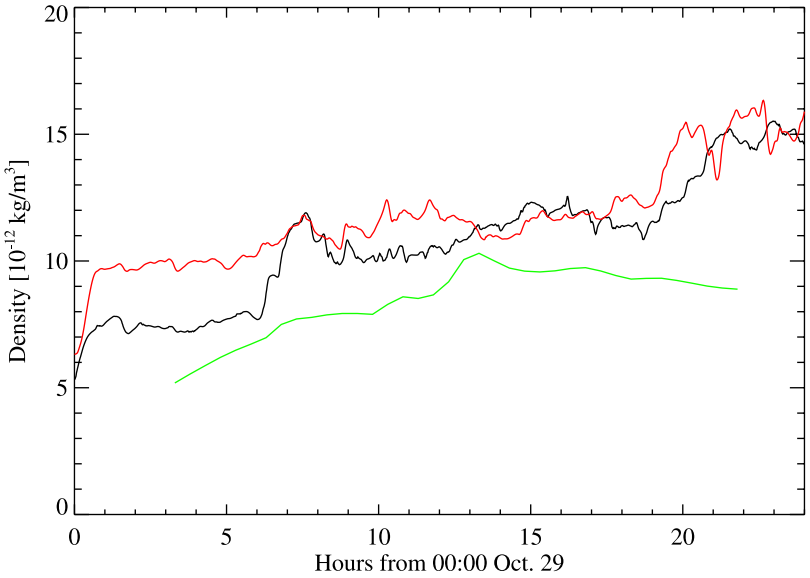

Figure 10. Comparison of the measured (black) and simulated (red and green) ion densities at the location of the Champ satellite. The red line shows a simulation with the thermosphere driven by AMIE data assimilation and the green line corresponds to the Sun-to-thermosphere simulation.

conditioning requires well resolved simulations over a long period and thus needs significant computational resources, even with very efficient codes. Third, we coupled the SC and IH models for all MHD parameters without any "renormalization."

[74] For the magnetosphere system the simulations proved that the coupled system behaves reasonably even under the most extreme conditions. The numerical schemes are robust enough to model the extremely strong CME shock and the following huge magnetic storm.

[75] A very important aspect of the complete Sun-to-thermosphere simulation was the resolution and speed. We note that this simulation involved over 160 million state variables. The active region on the Sun was resolved with grid size of 1/340 R_S, an unprecedented resolution in any global corona simulation. The heliosphere and the geospace was also resolved with good accuracy. On 256 CPUs of NASA's SGI Altix system (Columbia) the simulation ran slightly faster than real time. On the basis of our scaling curves we estimate that we can run a well-resolved Sun-Earth superstorm simulation about 1.5 faster than real time on 512 CPUs.

[76] On the basis of the experience gained with this simulation, we attempt to "design" a practical space weather modeling system, point out the critical problems and try to list what is needed to overcome these problems. A background code has to be driven by data that is available in (almost) real time, i.e., solar magnetograms. The background code has to run continuously on a computer that is large enough for real-time performance. This real-time run can involve only the SC + EE and IH components. When a CME is observed, a new eruption simulation has to be started on a much larger machine that allows faster than real-time performance. This may require grid computing technologies. Both the background and the eruption runs should initiate a CME automatically and almost instantaneously. This will probably require real-time vector magnetograms and a much better understanding of the CME initiation mechanisms. Once the CME is approaching the Earth in the faster than real time simulation, the GM, IM, IE, and UA components should be initialized using the IH data upstream of the Earth. Then one or more coupled IH, GM, IM, IE, and UA runs should be started in the vicinity of the location of the Earth. One may select the actual location of the Earth and a nearby location where the CME is strongest (say within a sphere). These simulations should run in parallel and provide some ensemble prediction for the effects on the Earth. If there are multiple CME eruptions in a short time interval, one may need to start a new "eruption" run while the previous "eruption" runs are still not completed. One thus needs a lot of computational resources for a fraction of the time, and some base computer continuously. The Center for Space Environment Modeling is working on several aspects of these problems, and we hope that first-principles physics-based space weather prediction will become a reality in the not too distant future.

[77] **Acknowledgments.** This work has been supported by NASA AISRP grant NNG04GP89G, NSF ITR project ATM-0325332, and by DoD MURI grant F49620-01-1-0359. We gratefully acknowledge the supercomputing resources provided by NASA's Columbia system under award SMD1-Dec04-0099. We acknowledge using the CME catalog that is

generated and maintained at the CDAW Data Center by NASA and Catholic University of America in cooperation with the Naval Research Laboratory. We also acknowledge the use of data from SOHO, ACE, and Geotail spacecraft. We thank Thomas Zurbuchen, Jim Raines, and Ruth Skoug for their help with the observational data. We thank Angelos Vourlidas for providing the LASCO C3 image of the CME. GT has been partially supported by the Hungarian Science Foundation (OTKA, grant T047042).

References

Barbieri, L. P., and R. E. Mahmot (2004), October–November 2003's space weather and operations lessons learned, *Space Weather*, *2*, S09002, doi:10.1029/2004SW000064.

De Zeeuw, D., S. Sazykin, R. Wolf, T. Gombosi, A. Ridley, and G. Tóth (2004), Coupling of a global MHD code and an inner magnetosphere model: Initial results, *J. Geophys. Res.*, *109*, A12219, doi:10.1029/2003JA010366.

Dryer, M., Z. Smith, C. D. Fry, W. Sun, C. S. Deehr, and S.-I. Akasofu (2004), Real–time shock arrival predictions during the ''Halloween 2003 epoch,'' *Space Weather*, *2*, S09001, doi:10.1029/2004SW000087.

Getley, I. L. (2004), Observation of solar particle event on board a commercial flight from Los Angeles to New York on 29 October 2003, *Space Weather*, *2*, S05002, doi:10.1029/2003SW000058.

Gombosi, T. I., G. Tóth, D. L. De Zeeuw, K. C. Hansen, K. Kabin, and K. G. Powell (2002), Semi-relativistic magnetohydrodynamics and physics-based convergence acceleration, *J. Comput. Phys.*, *177*, 176–205.

Gombosi, T. I., et al. (2004), Solution adaptive MHD for space plasmas: Sun-to-Earth simulations, *Comput. Sci. Eng.*, *6*, 14–35.

Gombosi, T. I., et al. (2006), Halloween storm simulations with the space weather modeling framework, in *Proceedings of 44th Aerospace Sciences Meeting*, *Pap. 2006-87*, Am. Inst. of Aeron. and Astron., Reno, Nevada.

Groth, C. P. T., D. L. De Zeeuw, T. I. Gombosi, and K. G. Powell (2000), Global 3D MHD simulation of a space weather event: CME formation, interplanetary propagation, and interaction with the magnetosphere, *J. Geophys. Res.*, *105*, 25,053–25,078.

Intriligator, D. S., W. Sun, M. Dryer, C. D. Fry, C. Deehr, and J. Intriligator (2005), From the Sun to the outer heliosphere: Modeling and analyses of the interplanetary propagation of the October/November (Halloween) 2003 solar events, *J. Geophys. Res.*, *110*, A09S10, doi:10.1029/2004JA010939.

Jackson, B. V., A. Buffington, P. P. Hick, X. Wang, and D. Webb (2006), Preliminary three-dimensional analysis of the helispheric response to the 28 October 2003 CME using SMEI white-light observations, *J. Geophys. Res.*, *111*, A04S91, doi:10.1029/2004JA010942.

Killeen, T., C. DeLuca, T. Gombosi, G. Tóth, Q. Stout, C. Goodrich, A. Sussman, and M. Hesse (2006), Integrated frameworks for earth and space weather simulation, paper presented at American Meteorological Society Meeting, Atlanta, Ga.

Krall, J., V. B. Yurchyshyn, S. Slinker, R. M. Skoug, and J. Chen (2006), Flux rope model of the 2003 October 28–30 coronal mass ejection and interplanetary coronal mass ejection, *Astrophys. J.*, *642*, 541–553.

Liu, Y., and K. Hayashi (2006), The 2004 October–November fast halo coronal mass ejections and the large scale magnetic field structures, *Astrophys. J.*, *640*, 1135–1141.

Lu, G., et al. (1998), Global energy deposition during the January 1997 magnetic cloud event, *J. Geophys. Res.*, *103*, 11,685–11,694.

Lugaz, N., W. B. Manchester, I. I. Roussev, G. Tóth, and T. I. Gombosi (2007), Numerical simulation of the homologous CMEs from active region 9236, *Astrophys. J.*, *659*, 788, doi:10.1086/512005.

Luhmann, J. G., S. C. Solomon, J. A. Linker, J. G. Lyon, Z. Mikic, D. Odstrcil, W. Wang, and M. Wiltberger (2004), Coupled model simulation of a Sun-to-Earth space weather event, *J. Atmos. Sol. Terr. Phys.*, *66*, 1243.

Lundstedt, H. (2006), The sun, space weather and GIC effects in Sweden, *Adv. Space Res.*, *37*, 1182–1191.

Manchester, W. B. (2001), The role of nonlinear alfven waves in shear formation during solar magnetic flux emergence, *Astrophys. J.*, *547*, 503–519.

Manchester, W. B. (2003), Buoyant disruption of magnetic arcades with self-induced shearing, *J. Geophys. Res.*, *108*(A4), 1162, doi:10.1029/2002JA009252.

Manchester, W. B., T. I. Gombosi, A. J. Ridley, I. I. Roussev, D. L. De Zeeuw, I. V. Sokolov, K. G. Powell, and G. Tóth (2004), Modeling a space weather event from the Sun to the Earth: CME generation and interplanetary propagation, *J. Geophys. Res.*, *109*, A02107, doi:10.1029/2003JA010150.

Manchester, W. B., T. I. Gombosi, D. L. De Zeeuw, I. V. Sokolov, I. I. Roussev, K. G. Powell, J. Kóta, G. Tóth, and T. H. Zurbuchen (2005), Coronal mass ejection shock and sheath structures relevant to particle acceleration, *Astrophys. J.*, *622*, 1225–1239.

Odstrcil, D., V. J. Pizzo, and C. N. Arge (2005), Propagation of the 12 May 1997 interplanetary coronal mass ejection in evolving solar wind structures, *J. Geophys. Res.*, *110*, A02106, doi:10.1029/2004JA010745.

Powell, K. G., P. L. Roe, T. J. Linde, T. I. Gombosi, and D. L. De Zeeuw (1999), A solution-adaptive upwind scheme for ideal magnetohydrodynamics, *J. Comput. Phys.*, *154*, 284–309.

Pulkkinen, A., S. Lindahl, A. Viljanen, and R. Pirjola (2005), Geomagnetic storm of 29–31 October 2003: Geomagnetically induced currents and their relation to problems in the Swedish high-voltage power transmission system, *Space Weather*, *3*, S08C03, doi:10.1029/2004SW000123.

Ridley, A. J., and E. Kihn (2004), Polar cap index comparisons with AMIE cross polar cap potential, electric field, and polar cap area, *Geophys. Res. Lett.*, *31*, L07801, doi:10.1029/2003GL019113.

Ridley, A. J., and M. W. Liemohn (2002), A model-derived storm time asymmetric ring current driven electric field description, *J. Geophys. Res.*, *107*(A8), 1151, doi:10.1029/2001JA000051.

Ridley, A. J., T. I. Gombosi, and D. L. De Zeeuw (2004), Ionospheric control of the magnetosphere: Conductance, *Ann. Geophys.*, *22*, 567–584.

Ridley, A. J., Y. Deng, and G. Tóth (2006), The Global Ionosphere-Thermosphere model, *J. Atmos. Sol. Terr. Phys.*, *68*, 839.

Riley, P., J. A. Linker, Z. Mikić, D. Odstrcil, V. J. Pizzo, and D. F. Webb (2002), Evidence of posteruption reconnection associated with coronal mass ejections in the solar wind, *Astrophys. J.*, *578*, 972–978.

Roussev, I., T. Gombosi, I. V. Sokolov, M. Velli, W. Manchester, D. De Zeeuw, P. Liewer, G. Tóth, and J. Luhmann (2003a), A three-dimensional model of solar wind incorporating solar magnetogram observations, *Astrophys. J.*, *595*, L57–L61.

Roussev, I. I., T. G. Forbes, T. I. Gombosi, I. V. Sokolov, D. L. De Zeeuw, and J. Birn (2003b), A three-dimensional flux rope model for coronal mass ejections based on a loss of equilibrium, *Astrophys. J.*, *588*, L45–L48.

Skoug, M., J. T. Gosling, J. T. Steinberg, D. J. McComas, C. W. Smith, N. F. Ness, Q. Hu, and L. F. Burlaga (2004), Extremely high speed solar wind: 29–30 October 2003, *J. Geophys. Res.*, *109*, A09102, doi:10.1029/2004JA010494.

Titov, V. S., and P. Dèmoulin (1999), Basic topology of twisted magnetic configurations in solar flares, *Astron. Astrophys.*, *351*, 701–720.

Toffoletto, F., S. Sazykin, R. Spiro, and R. Wolf (2003), Inner magnetospheric modeling with the Rice Convection Model, *Space Sci. Rev.*, *107*, 175–196.

Tóth, G. (2006), Flexible, efficient and robust algorithm for parallel execution and coupling of components in a framework, *Comput. Phys. Comm.*, *174*, 793.

Tóth, G., et al. (2005), Space Weather Modeling Framework: A new tool for the space science community, *J. Geophys. Res.*, *110*, A12226, doi:10.1029/2005JA011126.

Tóth, G., D. L. De Zeeuw, T. I. Gombosi, and K. G. Powell (2006), A parallel explicitimplicit time stepping scheme on block-adaptive grids, *J. Comput. Phys.*, *217*, 722, doi:10.1016j.jcp.2006.01.029.

Usmanov, A. V., and M. L. Goldstein (2003), A tilted-dipole MHD model of the solar corona and solar wind, *J. Geophys. Res.*, *108*(A9), 1354, doi:10.1029/2002JA009777.

Usmanov, A. V., M. L. Goldstein, B. P. Besser, and J. M. Fritzer (2000), A global MHD solar wind model with WKB Alfvén waves: Comparison with Ulysses data, *J. Geophys. Res.*, *105*, 12,675–12,695.

Wang, Y. M., P. Z. Ye, G. Zhou, S. J. Wang, S. Wang, Y. H. Yan, and J. X. Wang (2005), The interplanetary responses to the great solar activities in late October 2003, *Solar Phys.*, *226*, 337–357, doi:10.1007s11207-005-6877-2.

Webb, D. F., and J. H. Allen (2004), Spacecraft and ground anomalies related to the October–November 2003 solar activity, *Space Weather*, *2*, S03008, doi:10.1029/2004SW000075.

Wolf, R. A., M. Harel, R. W. Spiro, G. Voigt, P. H. Reiff, and C. K. Chen (1982), Computer simulation of inner magnetospheric dynamics for the magnetic storm of July 29, 1973, *J. Geophys. Res.*, *87*, 5949–5962.

Wu, S. T., W. P. Guo, D. J. Michaels, and L. F. Burlaga (1999), MHD description of the dynamical relationships between a flux rope, streamer, coronal mass ejection, and magnetic cloud: An analysis of the January 1997 Sun-Earth connection event, *J. Geophys. Res.*, *104*, 14,789.

Yang, G., Y. Xu, W. Cao, H. Wang, C. Denker, and T. Rimmele (2004), Photospheric shear flows along the magnetic neutral line of active region 10486 prior to an x10 flare, *Astrophys. J.*, *617*, L151–L154.

Zurbuchen, T. H., G. Gloeckler, F. Ipavich, J. Raines, C. W. Smith, and L. A. Fisk (2004), On the fast coronal mass ejections in October/November 2003: ACE-SWICS results, *Geophys. Res. Lett.*, *31*, L11805, doi:10.1029/2004GL019461.

D. L. De Zeeuw, T. I. Gombosi, W. B. Manchester, A. J. Ridley, I. V. Sokolov, and G. Tóth, Center for Space Environment Modeling, University of Michigan, Ann Arbor, MI, 48109-2143, USA. (gtoth@umich.edu)

I. Roussev, Institute for Astronomy, University of Hawaii at Manoa, Honolulu, HI 96822, USA.